Toward a Low-Cost Artificial Leaf: Driving Carbon-Based and Bifunctional Catalyst Electrodes with Solution-Processed Perovskite Photovoltaics

Tiva Sharifi, Christian Larsen, Jia Wang, Wai Ling Kwong, Eduardo Gracia-Espino, Guillaume Mercier, Johannes Messinger, Thomas Wågberg, and Ludvig Edman**

Molecular hydrogen can be generated renewably by water splitting with an "artificial-leaf device", which essentially comprises two electrocatalyst electrodes immersed in water and powered by photovoltaics. Ideally, this device should operate efficiently and be fabricated with cost-efficient means using earth-abundant materials. Here, a lightweight electrocatalyst electrode, comprising large surface-area $NiCo_2O_4$ nanorods that are firmly anchored onto a carbon–paper current collector via a dense network of nitrogen-doped carbon nanotubes is presented. This electrocatalyst electrode is bifunctional in that it can efficiently operate as both anode and cathode in the same alkaline solution, as quantified by a delivered current density of 10 mA cm^{-2} at an overpotential of 400 mV for each of the oxygen and hydrogen evolution reactions. By driving two such identical electrodes with a solution-processed thin-film perovskite photovoltaic assembly, a wired artificial-leaf device is obtained that features a Faradaic H_2 evolution efficiency of 100%, and a solar-to-hydrogen conversion efficiency of 6.2%. A detailed cost analysis is presented, which implies that the material-payback time of this device is of the order of 100 days.

1. Introduction

A global challenge is that the energy consumption is increasing at a rapid pace, while a majority of the current supply originates in the burning of nonrenewable fossil fuels, which contributes to global warming. Coupled with the progress of developing countries, where many users still are not connected to the electric grid, it is clear that alternative energy technologies are needed that can contribute with renewable fuels in significant amounts. In this challenging context, researchers have found inspiration in the process of natural photosynthesis when they attempt to convert the plentiful, but intermittent, solar irradiation incident on the Earth's surface into a storable fuel, using a range of methods commonly coined as artificial photosynthesis.[1–9]

One emerging technology to achieve such solar-to-fuel conversion is the "artificial-leaf device", which essentially comprises an assembly of photovoltaics (PVs) that drives two electrocatalyst electrodes immersed in water.[10–12] This device produces molecular hydrogen and oxygen using only sunlight and water as the input, and during the past few years its performance has improved drastically, with the current record for the solar-to-hydrogen (STH) conversion efficiency being above 10%.[13–16] It is, however, clear that in order to become truly sustainable and useful, the artificial-leaf device should comprise solely, or predominantly, earth-abundant materials and be produced with scalable and low-cost methods. Moreover, from a processing and transport point of view, it is preferable if it can be lightweight and flexible.

Perovskite materials[14,17–21] have recently emerged as an interesting option to incumbent silicon[15,20] and copper-indium-gallium-selenide[16,20] for the active material in PVs, due to a high and quickly improving solar-to-electric (STE) conversion efficiency and an opportunity for cost-efficient, solution-based fabrication.[17,18,21,23] The electrocatalyst electrode comprises a catalytically active material deposited on the surface of a current collector. Commonly employed materials for the current collector are bulk or porous metals,[15] whereas a popular choice for the catalyst is various types of metal-oxides.[24–38] From a system-cost and practicality perspective, it is desirable to develop a functional lightweight and low-cost current collector and to identify a catalyst that is bifunctional in that it can drive the oxygen evolution reaction (OER) and the hydrogen evolution reaction (HER) in the same water solution.[14,39–44]

Here, we present an artificial-leaf device that delivers an STH efficiency of 6.2% and a Faradaic H_2 evolution efficiency of 100%. We mention that our device is not fully integrated at this stage,

Dr. T. Sharifi, Dr. C. Larsen, Dr. J. Wang, Dr. E. Gracia-Espino, Dr. G. Mercier, Prof. T. Wågberg, Prof. L. Edman
Department of Physics
Umeå University
Umeå 90187, Sweden
E-mail: thomas.wagberg@umu.se; ludvig.edman@umu.se
Dr. W. L. Kwong, Prof. J. Messinger
Department of Chemistry
Umeå University
Umeå 90187, Sweden

DOI: 10.1002/aenm.201600738

as the PV assembly is wired to the electrocatalyst electrodes, and that such a wired system frequently has been described as PV-driven electrolysis in the scientific literature. We have nevertheless opted to term it an artificial-leaf device, on the basis of that all of the essential components of the integrated device are in place and that the complete integration should be relatively straightforward. The device comprises an assembly of solution-processed perovskite PVs, featuring an STE efficiency of ≈10%, which drives two identical electrocatalyst electrodes immersed into the same alkaline water solution. The bifunctional catalyst electrode consists of porous and polycrystalline $NiCo_2O_4$ nanorods, entangled with and attached to a nitrogen-doped carbon nanotubes (N-CNTs) network, which in turn is anchored onto a carbon paper (CP) current collector. At an overpotential of 400 mV, the catalyst electrode delivers a current density of 10 mA cm^{-2} for the anodic and cathodic reactions. This corresponds to a turn-over frequency per metal atom of 0.02 s^{-1} for oxygen evolution and 0.04 s^{-1} for hydrogen evolution. The presented lightweight artificial-leaf device represents a stepping stone toward future high-volume fabrication using earth-abundant and low-cost materials, as exemplified by that an accompanying cost analysis demonstrates that the material payback time for this free-standing fuel producer can be of the order of 100 days.

2. Results and Conclusion

2.1. The Electrocatalyst Electrode

The catalyst electrode was synthesized in a bottom-up process, and details on the fabrication process are available in the Experimental Section. In short, N-CNTs were grown on a CP substrate by chemical vapor deposition using a nanometer thin Fe/Ti bilayer as the catalyst/buffer material. The resulting N-CNT/CP structure was immersed into an aqueous solution, comprising cobalt nitrate, nickel nitrate, and urea, where it was hydrothermally treated at 120 °C. Nanorods were observed to form both on top of the N-CNT/CP and as dispersed material in the solution. At the conclusion of this growth process, the coated substrate and the dispersed nanorods were removed from the solution and separately heat-treated at 300 °C under ambient air.

The synthesized electrode was characterized with a wide range of methods, and **Figure 1**a presents a schematic of the derived morphology as a guide to the reader, where the larger (green) structures are nanorods and the flexible and thin (blue) structures are N-CNTs. Figure 1b is a scanning electron microscopy (SEM) image, which displays that each CP fibre is covered by a dense network of nanorods and N-CNTs. A higher-magnification SEM of the same fibre is shown in Figure 1c and it reveals an intimate intermixing of thin and flexible N-CNTs (diameter = 20–30 nm) with larger and needle-shaped nanorods (diameter = 30–100 nm). We propose that the intimate mixing is effectuated by that the dispersed N-dopant sites on the nanotubes function as effective anchoring points for the nanorods.[45,46] Moreover, at several locations it is observed that the N-CNTs penetrate through the nanorods (see also Figure S1, Supporting Information). Coupled with the firm attachment of the N-CNTs onto the CP substrate, it is clear that facile and stable charge-transport paths between the nanorods and the current collector are available. We also wish to mention that N-CNTs, despite a larger number of functional defects, have been shown to feature a higher conductivity than undoped CNTs.[47]

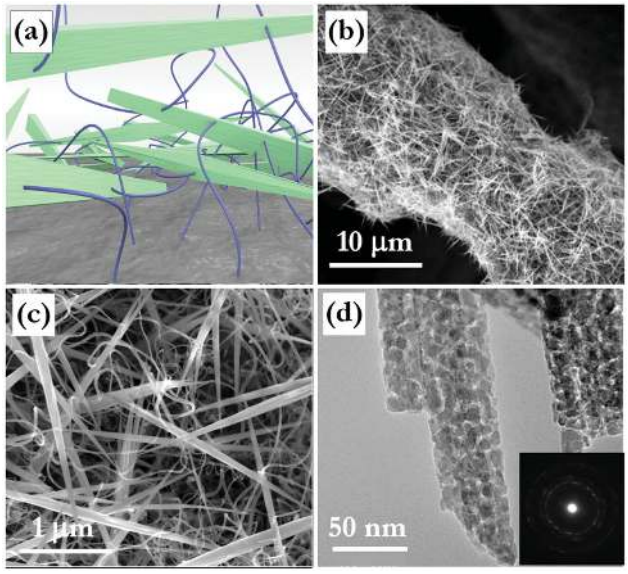

Figure 1. a) Schematic of the morphology of the catalyst electrode, displaying thin and flexible (blue) N-CNTs anchored onto a (grey) CP substrate, between which needle-shaped (green) nanorods are dispersed. b) SEM image of the catalyst electrode structure, showing a CP fibre densely coated with N-CNTs and nanorods. c) High-magnification SEM image of the electrode structure, displaying a well-blended mixture of flexible N-CNTs and rigid and needle-shaped nanorods. d) High-resolution transmission electron microscopy image displaying the rough surface of isolated nanorods. Inset: the electron diffraction pattern of isolated nanorods.

Figure 1d is a high-resolution transmission electron microscopy image of a small number of solution-grown nanorods, which demonstrates that the nanorods exhibit a rough surface. The corresponding electron diffraction pattern in the inset displays a series of dots positioned in concentric rings, which implies a polycrystalline nanorod structure. The combination of a well-dispersed morphology and a rough surface is concomitant with a large nanorod surface area, which is an attractive feature of a catalyst material.

The elemental composition of the catalyst electrode was measured to be Ni, Co, O, N, and C using energy dispersive X-ray spectroscopy (Figure S2, Supporting Information) and X-ray photoelectron spectroscopy (Figure S3a, Supporting Information). The Raman spectra of the solution-grown nanorods and the catalyst electrode are depicted in **Figure 2**a. For the solution-grown nanorods (top trace), we identify four distinct features centred at 184, 475, 562, and 639 cm^{-1}. These positions correlate perfectly with those reported in the literature for the F_{2g}, E_g, F_{2g}, and A_{1g} vibrational modes of $NiCo_2O_4$.[29] The same $NiCo_2O_4$ peaks are also observed for the catalyst electrode (bottom trace), although they are broadened and slightly downshifted in comparison to the solution-grown nanorods. We assign this spectral change to the observed direct interactions between the $NiCo_2O_4$ nanorods and the N-CNTs in the catalyst

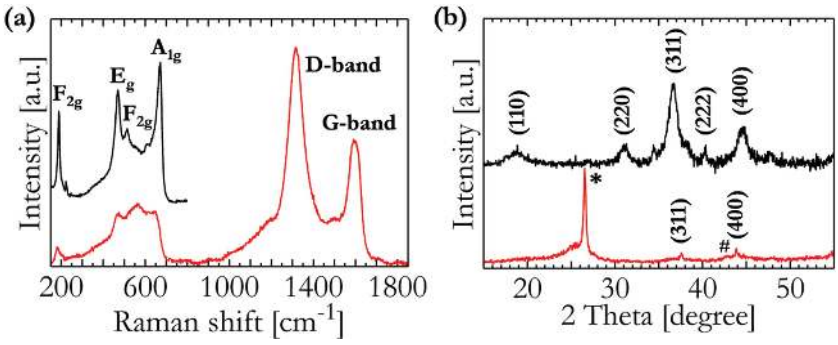

Figure 2. a) Raman spectra with assigned vibrational modes of the solution-grown nanorods (top) and the catalyst electrode (bottom). b) XRD patterns of the solution-grown nanorods (top) and of the catalyst electrode (bottom). The identified $NiCo_2O_4$ planes are indicated, while the (002) and (100) planes of the N-CNTs in the electrode are marked with (*) and (#), respectively.

electrode (see Figure 1).[48–51] The presence of N-CNTs in the catalyst electrode is manifested in the characteristic D-band and G-band at 1390 cm^{-1} and 1650 cm^{-1}, respectively.[52]

The X-ray diffraction data (XRD) of the solution-grown nanorods (Figure 2b, top trace) are in good agreement with literature values for a $NiCo_2O_4$ spinel structure.[48,51,53] For the catalyst electrode (bottom trace), the data are dominated by the (002) and (100) reflections from the N-CNTs (marked by * and #, respectively), although the (311) and (400) $NiCo_2O_4$ reflections are also distinguishable.[54,55] The conclusion is thus that the nanorods exist in a polycrystalline spinel $NiCo_2O_4$ structure, and that they are well-dispersed and well-anchored onto the N-CNTs.

For the investigation of the electrochemical properties, the $NiCo_2O_4$/N-CNT/CP electrode was cut into the desired shape and size and then immersed into an aqueous 0.1 M KOH solution (pH = 13). For comparison, bare CP and N-CNT/CP electrodes of the same size were prepared and characterized under identical conditions. **Figure 3** presents linear sweep voltammetry (LSV) data obtained in the HER (left) and the OER (right) regime. All potentials are reported with respect to the reversible hydrogen electrode (RHE), resulting in that the

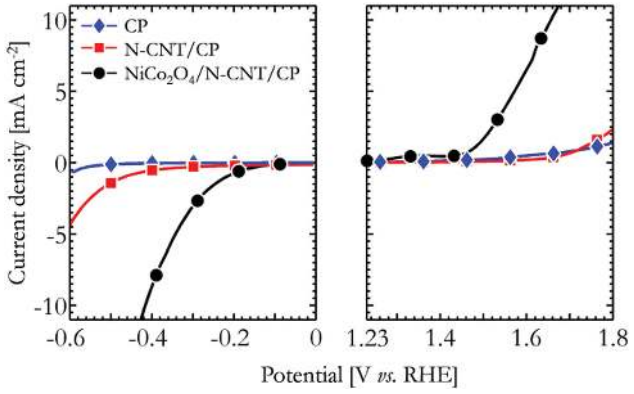

Figure 3. Linear sweep voltammetry in the hydrogen-evolution (left) and the oxygen-evolution (right) regime. The investigated working electrodes are CP (blue diamonds), N-CNT/CP (red squares), and $NiCo_2O_4$/N-CNT/CP (black circles). The scan rate was 2 mV s^{-1} and the electrolyte was 0.1 M KOH aqueous solution.

"zero overpotential" points for the HER and OER are 0 and 1.23 V versus RHE, respectively. While both the CP and the N-CNT/CP electrodes featured low current density, i.e., poor catalytic activity, over the probed voltage range, the $NiCo_2O_4$/N-CNT/CP electrode in contrast displayed a high catalytic activity for both hydrogen and oxygen evolution. This capacity of the catalyst electrode is quantified by that the overpotential η required to reach a current density of 10 mA cm^{-2} is η_{OER} = 0.42 V for oxygen evolution and η_{HER} = 0.41 V for hydrogen evolution. These data thus demonstrate that the $NiCo_2O_4$ nanorod coating on the N-CNT/CP electrode is catalytically active and that it is electrically well connected to the CP current collector, which is in good agreement with the structural analysis.

The temporal stability of the electrocatalyst electrode during operation was measured with a variety of techniques. The morphology and structure before and after a long-term constant-voltage operation were probed by X-ray photoelectron spectroscopy (XPS) (Figure S3b, Supporting Information), SEM (Figure S4, Supporting Information), and Raman spectroscopy (Figure S5, Supporting Information), and the observed essential invariability suggests that the electrocatalyst electrode structure is highly robust. The temporal evolution of the electrolysis current was measured, and data for the HER current (at −0.4 V vs RHE) and the OER current (at +1.7 V vs RHE) are presented in **Figure 4**a,b, respectively. We find that the HER current increases by 5% following more than 4 h of uninterrupted operation, whereas the OER current drops by 15% over the same time span.

To probe whether the entire measured current is due to hydrogen and oxygen gas evolution at the anode and cathode, respectively, we performed membrane-inlet mass spectrometry experiments. Figure 4c presents the accumulated amount of hydrogen gas (open white circles) and oxygen gas (solid red circles) as a function of time, with the accompanying solid lines indicating the theoretical limits. The good match between the measured and theoretical values for the hydrogen gas evolution demonstrates that the cathodic H_2 production occurs with 100% Faradaic efficiency (see also right axis in Figure 4c). By contrast, the 85% Faradaic efficiency for O_2 production on the anodic side indicates that some of the oxidation current is caused by an alternative side reaction. Potential side-reaction culprits are hydrogen peroxide formation or the oxidation of the N-CNT/CP electrode support, although we in the latter context mention that we were unable to detect any accumulation of carbon dioxide in the headspace. Further experiments will be required to identify and eliminate the side reaction.

With the values for the Faradaic efficiency at hand and by measuring the nanorod loading on the electrode to 0.3 mg cm^{-2} with thermogravimetric analysis, we can calculate the turnover frequency (TOF) per transition metal atom (Ni, Co). At a current density of 10 mA cm^{-2} (i.e., at an overpotential of $\eta \approx 400$ mV), we find that the TOF is 0.018 s^{-1} for the anodic OER and 0.042 s^{-1} for the cathodic HER. As

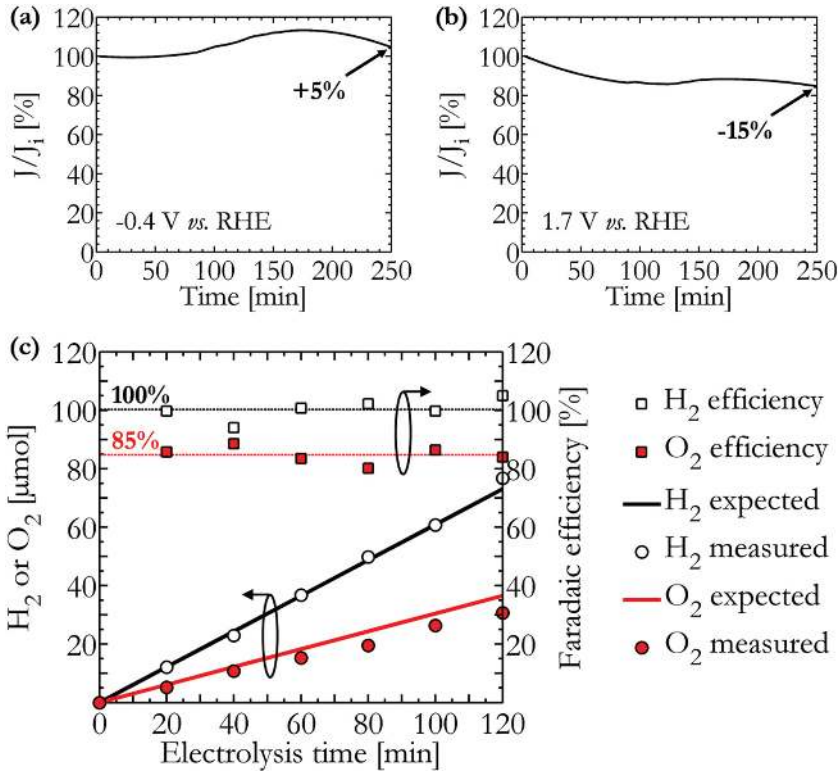

Figure 4. Long-term current stability of the $NiCo_2O_4$/N-CNT/CP catalyst electrode for a) hydrogen evolution at –0.4 V versus RHE and b) oxygen evolution at +1.7 V versus RHE. The measurements were executed in a three-electrode LSV setup, with the catalyst electrode immersed in 0.1 M KOH aqueous solution. c) The accumulated amounts of evolved H_2 gas (open white circles) and O_2 gas (solid red circles) from constant-current-driven catalyst electrodes, as measured by membrane-inlet mass spectrometry. The solid lines indicate the theoretical upper limit for the gas evolution reactions. The corresponding Faradaic efficiencies of the H_2 evolution (open white squares) and the O_2 evolution (red solid squares) reactions are indicated by the right y-axis. The catalyst electrodes were immersed in 0.1 M KOH aqueous solution and driven by 10 mA cm^{-2}.

this calculation is based on the assumption that the entire nanorod coating is catalytically active, the presented values represent a lower limit.[56]

Table S1 (Supporting Information) presents a summarizing comparison of the published capacity of bifunctional catalyst materials deposited on either carbon-based or metallic current collectors for water electrolysis. We find that our catalyst electrode displays a similar or better performance than a majority of the other bifunctional catalysts deposited on a carbon-based current collector during operation in 0.1 M KOH aqueous solution (pH 13), as exemplified by that it delivered a lower overpotential by >100 mV for both OER and HER in comparison to a $NiCo_2O_4$ electrocatalyst deposited on glassy carbon current collector.[27,29,57–62] There are however other catalyst materials deposited on metal-based current collectors (or operating at a higher pH) that feature a lower overpotential at the same drive current, but it is anticipated that such metal-based electrodes will carry a much higher price and larger weight than the carbon-based electrode used in our study. In this context, we also mention that the metal loading on our catalyst electrode is relatively low, and attribute its high catalytic activity to the large surface area of the $NiCo_2O_4$ nanorods and the direct and stabile electronic transport paths between the nanorods and the CP current collector as facilitated by the N-CNTs.

2.2. The Perovskite Photovoltaic and the Artificial Leaf Device

The device structure of the perovskite PV is shown in **Figure 5**a. It was fabricated on a glass substrate coated with indium-tin-oxide (ITO) as the transparent anode. Layers of poly(3,4-ethylenedioxythiophene):poly(styrene sulfonate) (PEDOT:PSS), $CH_3NH_3PbI_{3-x}Cl_x$ perovskite, and [6,6]-phenyl C_{61} butyric acid methyl ester (PCBM) were sequentially deposited from solution on top of the ITO anode, followed by physical vapor deposition of a set of four Al cathodes. The complete device was encapsulated between two glass plates, using a procedure outlined in Ref. [63] to allow for ambient-air operation. More details on the fabrication procedure can be found in the Experimental Section.

The perovskite PV exhibits broad-range absorption. Specifically, Figure 5b shows that >50% of the incident photons in the wavelength range between 340 and 750 nm are absorbed and transformed into electrons exiting the device structure, and that the peak external quantum efficiency is 81% at 510 nm. The performance of a typical perovskite PV under 1 sun illumination and in darkness is presented in Figure 5c. Our champion device featured a short-circuit current density of 19.5 mA cm^{-2}, an open-circuit voltage of 1.00 V, a fill factor of 59%, and an STE conversion efficiency of 11.5%. In total we have tested 60 perovskite PVs, and the average STE efficiency is 9.4 ± 1.0%.

The wired artificial-leaf device was fabricated by connecting a number of perovskite PV cells positioned on the same glass substrate in series, and allowing this integrated PV assembly to drive two catalyst electrodes immersed in a 0.1 M KOH aqueous solution. **Figure 6**a presents a photograph of an operating artificial-leaf device, with the illuminated PV assembly positioned to the left and the two water-immersed catalyst electrodes producing H_2 and O_2 gas localized to the right. A video of an operating device producing hydrogen gas is available in the Supporting Information. As observed in the photograph and video, we have opted to not include a membrane to separate the anode and cathode compartments, which might result in other reactions, e.g., reduction of dissolved O_2 at the cathode.

The "operation point" of the artificial-leaf device is given by the current (I) and voltage (V) combination generated by the PV assembly, which can be "consumed" by the catalyst electrodes. In Figure 6b, we have (in red) plotted the I–V relationships for perovskite PV assemblies comprising two, three, or four serially connected perovskite-PV cells with a

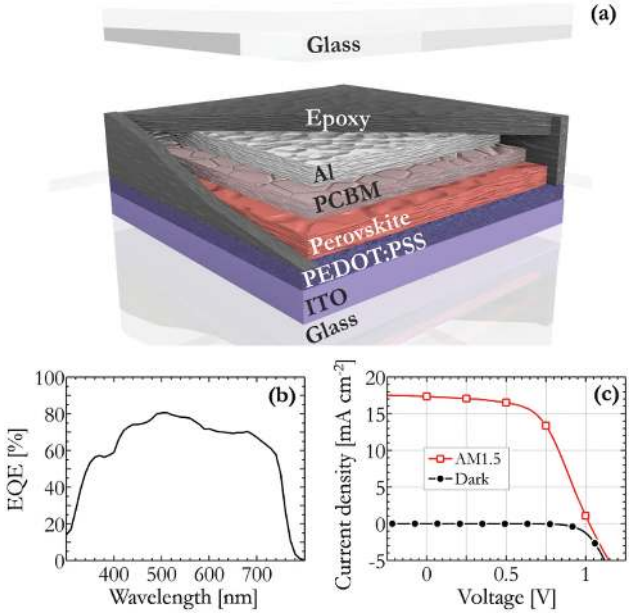

Figure 5. a) The schematic device structure of the thin-film perovskite PV, as protected from ambient air by two epoxy-attached glass plates. b) The measured external quantum efficiency as a function of wavelength, and c) the current density versus voltage for a perovskite PV during operation under 1-sun (AM1.5) illumination and in darkness.

constant total photoactive area of A_{PV} = 1 cm^2. The selection of a constant total PV area in the analysis is motivated by that we believe that one limiting factor for artificial-leaf devices in the future will be the footprint area occupied by the PVs. In this scenario, the implications are that with increasing number of serially connected PV cells, the delivered maximum current from the PV assembly will decrease, while the generated maximum voltage will increase. The *I*–*V* relationship for the catalyst-electrode (in blue) was measured in a two-electrode setup, with the area for each catalyst-electrode being A_{CAT} = 0.2 cm^2; the presented values for other catalyst-electrode areas were derived from these data through area renormalization.

As the theoretical lower voltage limit for water splitting is +1.23 V, it is clear from the perovskite-PV data presented in Figure 5c that at least two serially connected perovskite PVs are required in order to produce hydrogen gas. The operating point of the artificial-leaf device is provided by the intersection of the PV and catalyst-electrode curves in Figure 6b, and for the 2-serial-PV assembly we find low values for the operating current (I_{OP}) for all reasonable catalyst-electrode areas. A significant improvement is attained for the 3-serial-PV assembly, where the highest overall values for I_{OP} are attained at catalyst-electrode areas larger than 0.3 × A_{PV}. For smaller catalyst-electrode areas, the highest I_{OP} is instead achieved for the 4-serial PV assembly.

In Figure 6c, we have plotted data for I_{OP} as a function of the ratio between the catalyst-electrode area and the total area of the PV assembly. The STH conversion efficiency is directly dependent on I_{OP} in accordance with the equation

$$\eta_{STH} = \frac{E_{0,H_2O} \times I_{OP} \times \eta_{H2}}{P_{in} \times A_{PV}} \quad (1)$$

where $E_{0,\,H2O}$ is the thermodynamic potential for water-splitting (= 1.23 V), η_{H2} is the Faradaic efficiency for H_2 gas evolution (measured to be ≈100%; see Figure 4c and related discussion), P_{in} represents the power density of solar radiation incident on the PVs (here, 100 mW cm^{-2}), and A_{PV} is the total active area of the PV assembly.[64]

The STH conversion efficiency is presented by the right y-axis in Figure 6c, and the highest available value (as indicated by the horizontal solid black line) for reasonable values of the area of the catalyst electrode is achievable when the artificial leaf is driven by a 3-serial perovskite-PV assembly. Moreover, the STH efficiency and I_{OP} are found to improve with increasing catalyst area in an asymptotic manner, which implies that the device performance is rather robust to variations in the effective active areas of the PV assembly and the catalyst electrodes close to the peak operation point. The device displayed in Figure 6a featured a 3-serial perovskite PV assembly and an A_{CAT}/A_{PV} ratio of 0.20 cm^2/0.12 cm^2 = 1.67, which resulted in an STH efficiency of 6.2%; this particular data point is marked with an "x" in the graph in Figure 6c.

Grätzel and co-workers recently reported an artificial-leaf device delivering a notably high STH efficiency of 12.3%.[14] Their device comprised a perovskite PV assembly (STE efficiency = 17.3%) driving two catalyst electrodes composed of a NiFe layered double hydroxide deposited on a Ni-foam current collector immersed in an alkaline (1 M) KOH aqueous electrolyte. They selected to employ a very large relative active area of the catalyst with respect to the PV of ≈16 (whereas we used 1.67), which in combination with the highly alkaline solution resulted in a low overpotential for the HER and OER reactions. As a consequence, their device could be driven by a 2-serial PV architecture, which is attractive from an efficiency viewpoint, as indicated in Figure 6b.

The stability of our artificial-leaf device was investigated under both continuous and pulsed illumination. The former data are presented in Figure S6 (Supporting Information), and reveal that the operating current has dropped by 7% after 30 min of continuous operation, and that the decline thereafter accelerates. During pulsed illumination, as displayed in Figure 6d, the device stability is improved, and apart from a minor drop during the first two 1-min pulses the current remains constant throughout the test. Following systematic long-term testing of both the catalyst electrode (Figure 4a,b) and the PV device (Figure S7, Supporting Information), we draw the conclusion that the main stability limiter for our wired artificial-leaf device at this stage is the perovskite PV; more specifically, it is the morphology of the active material of the perovskite PV that is degrading, as evidenced by the drop in the short-circuit current density during device operation. We note that others have reached the same conclusion,[13,65] and that a large effort is aimed toward resolving this issue in the perovskite-PV community,[65–68] with successful efforts being aimed at improving the crystallinity of the active layer through the employment of mixed organic cation perovskites,[64] and the inclusion of a metal oxide layer between the active material and the cathode.[65] It is our intention to investigate whether these approaches can result in a stabilization of our artifical leaf device.

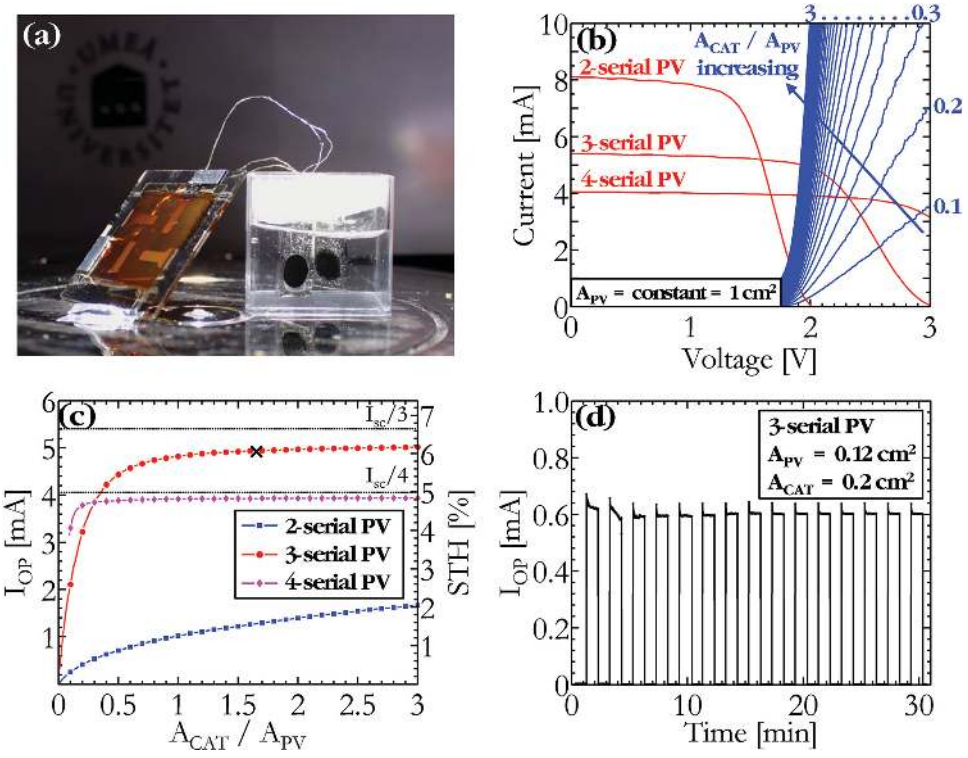

Figure 6. a) Photograph of an artificial-leaf device, comprising three serially connected perovskite PVs driving two identical electrocatalyst electrodes during the production of hydrogen and oxygen gas. b) The *I–V* graphs for a perovskite PV assembly, comprising two, three, or four serially connected cells, and for an electrocatalyst electrode. The total area of the PV assembly is constant at A_{PV} = 1 cm^2, while the catalyst-electrode area was varied as indicated by the arrow. c) The operating current of the artificial-leaf device as a function of the ratio between the catalyst-electrode area and the total PV assembly area. The right axis presents the corresponding STH efficiency values, while the black dotted lines indicate the maximum operating current for each PV assembly. The operation point for the artificial-leaf device presented in the photograph in (a) is marked with 'x'. d) The operating current of an artificial-leaf device as a function of time, during pulsed 1-sun (AM1.5) illumination, with the pulse duration being 1 min and the duty cycle being 50%.

For artificial-leaf devices to become useful and common commodities, it is fundamental that they are developed so that they can carry a competitive price tag. In order to evaluate the prospects of our artificial-leaf device in this context, we have performed an analysis of the materials costs and the material-payback time for our "current lab-scale fabrication" of devices and following a ramp up in a "future high-volume fabrication" scenario. For this end, we assume that we can achieve long-term stability of the device without significantly increasing the material costs.

The breakdown of the material costs for our current lab-scale fabrication is displayed in Tables S2 and S3 (Supporting Information) for the catalyst electrode and the perovskite PV, respectively. The presented data are either the actual costs for materials in our laboratory or, when that value is not available, taken from the literature. In this analysis, we have also considered the total amount of material consumed during the different fabrication processes, i.e., we have also accounted for material losses during manufacturing. As expected, we find that material cost per substrate area in our current processing method is very high at: \$1 800 m^{-2} for the catalyst electrode and \$5 200 m^{-2} for the perovskite PV. For the catalyst electrode, the major cost drivers are the nickel nitrate, the carbon paper, the Ti and Fe catalysts for producing the N-CNTs, and the cobalt nitrate in that order. For the perovskite PV, the major cost is attributed to the ITO-coated glass substrate, with additional significant contributions originating from the perovskite precursors and PCBM.

By defining a geometric fill factor (GFF) to account for the coverage of active device material on the substrate, we find that the catalyst electrode carries a cost-per-area (CPA) of CPA_{CAT} = \$2 300 m^{-2}, while the perovskite PV features a very high CPA_{PV} = \$289 000 m^{-2}, due to the low GFF (= 1.8%) of our employed PV architecture. With this information at hand, we can calculate the cost-per-area for the artificial-leaf device using the equation

$$CPA_{ALD} = \frac{A_{PV}CPA_{PV} + 2A_{CAT}CPA_{CAT}}{A_{PV}} \quad (2)$$

where the "2" is included to account for that the artificial-leaf device comprises two catalyst electrodes (anode and cathode). We also call attention to that we have opted to normalize the artificial-leaf device cost by the total PV area, as we are of the opinion that the footprint area occupied by the PVs will be a limiting factor in the future. With a selected A_{CAT}/A_{PV} ratio of 1.67, we find that CPA_{ALD} is a staggering \$297 000 m^{-2} for our current lab-scale devices.

This value is obviously not commercially viable, and in order to better evaluate the potential of the artificial-leaf device

technology, we have also listed projected material costs in a "future high-volume fabrication" scenario in Tables S4 and S5 (Supporting Information). The presented data are either current high-volume prices taken from commercial vendors' official listings or projections inspired by principles outlined in Refs. [69–71]. Moreover, as a future high-volume fabrication preferably should be executed in a solution-based roll-to-roll process, we anticipate that the PV substrate will be shifted from rigid glass to flexible polyethylene terephthalate, that solution-processed Ag has replaced ITO as the transparent PV anode, and that the PV cathode is shifted from thermally evaporated Al to a solution-processed ZnO/Ag bilayer.[72] We also anticipate that the GFF will be increased to 95% for both the catalyst electrode and the perovskite PV.

For the high-volume scenario, we find that the areal cost for the catalyst electrode is much lower at \$6.6 m^{-2}, with the major costs being assigned to the nickel nitrate, the carbon paper, and the pyridine precursor. The areal cost for the perovskite PV has dropped even more significantly to \$15.6 m^{-2}, and here we identify the Ag electrodes and the flexible barriers as the most expensive constituents. By using Equation (2), we find that the areal cost of the artificial-leaf device now is a mere CPA_{ALD} = \$38 m^{-2} (at A_{CAT}/A_{PV} = 1.67).

An important commercial viability metric is the cost-per-fuel weight (CPF_W). "The Fuel Cell Technologies Office" and "The Office of Energy Efficiency and Renewable Energy" have announced a roadmap, which states that in order for the artificial-leaf device technology to become competitive the CPF_W should be \$17.30 kg^{-1} H_2 in 2015 and \$5.70 kg^{-1} H_2 in 2020; and with the ultimate target being \$2.10 kg^{-1} H_2.[73,74] With this information at hand, we derived the following equation for the calculation of the material-payback time of our artificial-leaf device

$$t_{payback} = \frac{CPA_{ALD}}{CPF_W} \times \frac{e}{j_{OP,PV}} \times \frac{Z}{\eta_{H2}} \times \frac{N_A}{M_{W,H2}} \quad (3)$$

where e is the elementary charge, $j_{OP,PV}$ is the operating current density of the PV, $M_{W,H2}$ is the molecular weight of the hydrogen fuel (2 g mol^{-1}), N_A is Avogadro's constant, and Z accounts for the number of electrons consumed to form one fuel molecule (for H_2, Z = 2). For $j_{OP,PV}$ = 5 mA cm^{-2} and CPF_W = \$17.30 kg^{-1} H_2, we find that the material-payback time for our artificial-leaf device is 49 days. If we instead employ the ultimate \$2.10 kg^{-1} H_2 target for CPF_W, we find that the material payback time is a still reasonable 400 days. It is notable that we employed the future material cost for CPA_{ALD} in the above calculations, and that this value, for simplicity, does not account for additional costs for, e.g., equipment, personnel, and gas handling. It is also clear that it is critical to improve upon the stability of the perovskite PV so that it at least exceeds the material payback time. Finally, we wish to acknowledge that the employment of lead (in the active material of the perovskite PV) obviously is nondesirable from a health and environmental perspective, but that recent studies indicate that an essentially complete recycling of the lead can be attained from such PV devices through dissolution in a well-designed solvent and subsequent electrochemical plating.[65]

3. Conclusions

We present the synthesis and characterization of a light-weight and flexible electrocatalyst electrode comprising high-surface-area $NiCo_2O_4$ nanorods attached to a carbon-paper current collector via a network of nitrogen-doped carbon nanotubes. The catalyst electrode features a bifunctional activity at alkaline pH, as manifested by the production of both oxygen gas and hydrogen gas at a current density of 10 mA cm^{-2} at an overpotential for each reaction of ≈400 mV. An artificial-leaf device was constructed by allowing an assembly of three serially connected perovskite photovoltaics to drive two catalyst electrodes immersed in water, and under 1 sun illumination such a device delivers hydrogen gas at 100% Faradaic efficiency with a solar-to-hydrogen efficiency of 6.2%. A cost analysis suggests that the material-payback time for this lightweight artificial leaf can become of the order of 100 days.

4. Experimental Section

The Electrocatalyst Electrode: Thin layers of Ti buffer (10 nm) and Fe catalyst (5 nm) were sequentially thermally evaporated (Kurt J. Lesker PVD 75) onto a carbon paper (CP; ≈15 mΩ cm, SIGRACETGDL 10AA, Ion power, GER). The coated CP substrate was transferred to a chemical vapor deposition (CVD) chamber and heated to 800 °C under Varigon gas. Ammonia gas was injected into the CVD chamber at 25 mL min^{-1} for 15 min, and then pyridine was injected at 8 µL min^{-1} for 60 min using a syringe pump (NEMSYS, Cetoni). Thereafter, the substrate was allowed to cool to room temperature under Ar gas. At the end of this process, a nitrogen-doped carbon nanotube (N-CNT) network was observed to have formed on the CP substrate. The N-CNT/CP structure was immersed vertically into the teflon container of an autoclave, which was filled with 30 mL aqueous solution, comprising 0.7×10^{-3} M cobalt nitrate ($Co(NO_3)_2$-hexahydrate, Sigma Aldrich), 0.4×10^{-3} M nickel nitrate ($Ni(NO_3)_2$-hexahydrate, Sigma Aldrich), and 2×10^{-3} M urea (CH_4N_2O, Sigma Aldrich). The autoclave was maintained at 120 °C for 12 h, where after the substrate and the solution first were separately washed with water and ethanol and then heat treated under air at 300 °C for 2 h. This resulted in the formation of the $NiCo_2O_4$/N-CNT/CP catalyst electrode and $NiCo_2O_4$ nanorods dispersed in the synthesis solution.

The catalyst electrode was characterized with scanning electron microscopy (Zeiss Merlin FEG-SEM, acceleration voltage = 40 kV, beam current = 150 pA), high-resolution transmission electron microscopy (JEOL 2100F, voltage = 200 keV), Raman spectroscopy (Renishaw InVia Raman spectrometer, laser excitation wavelength = 785 nm), X-ray diffraction (Siemens D5000 X-ray diffractometer, Cu-Kα radiation, step size = 0.03°), X-ray photoemission spectroscopy (Kratos axis ultradelay-line detector electron spectrometer, monochromatic Al K_α source, power = 150 W), and thermogravimetric analysis (Mettler Toledo thermal gravimetric analysis/differential scanning calorimetry 1 LF/948, heating rate = 10 °C min^{-1}; end temperature = 950 °C).

For the LSV measurements, the working electrodes were prepared by cutting the as-fabricated CP, N-CNT/CP, and $NiCo_2O_4$/N-CNT/CP materials into a desired size. The WE was attached to a regular piece of glass with double-sided tape, with an Ag wire being included between the CP and the tape for external electric contacting. The wire and the WE edges were covered with an epoxy resin so that the active area of the WE exposed to the electrolyte was 0.2 cm^2. The WE, a Pt rod counter electrode, and a Ag/AgCl reference electrode were immersed into a 0.1 M KOH aqueous electrolyte (pH = 13), where the LSV scans were recorded at a scan rate of 2 mV s^{-1}. The Ag/AgCl reference potential ($E_{Ag/AgCl}$) was converted to the reversible hydrogen electrode potential (E_{RHE}) using the equation

$$E_{RHE} = E_{Ag/AgCl} + 0.222 + 0.059 \times pH \quad (4)$$

The 2-electrode current–voltage (*I–V*) data were recorded at a 1 cm interelectrode distance, using a parameter analyzer (Keithley 4200-SCS) operating at a sweep rate of 2 mV s^{-1}.

The amount of gas generated by the catalyst electrode during electrolysis was measured with membrane-inlet mass spectrometry. An airtight two-compartment reactor was used, where each compartment contained a catalyst electrode (one as the working electrode and the other as the counter electrode). The compartments, separated by a glass-frit, were filled with 0.1 M KOH aqueous electrolyte. Prior to the measurement, the electrolyte and the headspace of the reactor were purged with N_2 gas for 1 h, and subsequently the gas in the reactor (headspace and electrolyte) was measured for a period of 1 h to establish a baseline. The measurement was performed by applying a constant current density (10 mA cm^{-2} and –10 mA cm^{-2} for O_2 and H_2 detection, respectively) between the two electrodes for 2 h. For every 20 min of the 2 h electrolysis, 100 µL of gas was extracted from the headspace of the working compartment using a gas-tight syringe (VICI 050025) and injected into the entry port of a membrane-inlet mass spectrometer (ThermoFinnigan Delta plus XP) for measurement. The total amount of gas generated during the electrolysis was the sum of the gas measured in the headspace of the working compartment and the dissolved gas in the electrolyte, as calculated using Henry's law.[75] The response of the spectrometer toward O_2 and H_2 were calibrated by injections of known amounts of ambient air and 5% H_2 in Ar, respectively. For the O_2 measurement, the setup for both the reactor and the entry port of the spectrometer were positioned in a N_2-filled glove box (VAC, Omni-Lab Systems) to exclude contamination of external O_2.

The Perovskite Photovoltaic and the Artificial-Leaf Device: Patterned ITO-coated glass substrates (20 Ω per square, Thin Film Devices, USA) were cleaned by subsequent 10 min ultra-sonication in detergent (Extran MA01):deionized water mixture (1:10 volume ratio), deionized water, acetone, and isopropyl alcohol. The cleaned substrates were blown dry with compressed air and stored in an oven at 120 °C. Immediately prior to device fabrication, the ITO-coated substrates were exposed to UV-ozone for 10 min in a UVO-cleaner (42-220, Jelight Company). A PEDOT:PSS dispersion (Clevios P VP Al 4083, Heraeus) was filtered (pore size = 0.45 µm, Millex-HA, Merck) and then spin-coated onto the ITO substrate (spin speed = 4000 rpm, acceleration = 1000 rpm s^{-1}, time = 60 s). The PEDOT:PSS film (dry thickness = 35 nm) was annealed on a hotplate at 120 °C for 1 h. The coated substrate was thereafter transferred into a N_2-filled glove-box ($[O_2]$, $[H_2O]$ < 1 ppm), where the remaining fabrication procedure was executed.

The perovskite precursors, methyl ammonium iodide (MAI, LumTech) and lead(II) choride ($PbCl_2$, LumTech), were separately dissolved in dimethyl formamide (DMF, anhydrous, Sigma-Aldrich) in a concentration of 3 mmol mL^{-1}, and then mixed together at a {MAI : PbCl2} molar ratio of {3 : 1}. The precursor-blend solution was stirred at 60 °C in a N_2-filled glove box overnight. The blend solution was thereafter filtered through a 1.0 µm polytetrafluorethylene (PTFE) filter (Whatman) and a 0.45 µm PTFE filter (Puradisc 25 TF, VWR), and spin-coated on top of the PEDOT:PSS layer (spin speed = 4000 rpm, acceleration = 4000 rpm s^{-1}, time = 20 s). The 300 nm thick active-material film was annealed at 90 °C for 90 min, after which its color had turned dark brown. [6,6]-Phenyl-C_{61}-butyric acid methylester (PCBM, >99.5%, Solenne) was dissolved in chlorobenzene (Anhydrous, Sigma-Aldrich) in a concentration of 20 mg mL^{-1} and the solution was stirred on a magnetic hotplate at 60 °C for 3 h. The PCBM solution was filtered (PTFE filter, 0.45 µm, Puradisc 25 TF, VWR) and then spin-coated (spin-speed = 1000 rpm, acceleration = 1000 rpm s^{-1}, time = 60 s) on top of the perovskite layer. The thickness of the PCBM layer was 55 nm.

Four Al top electrodes (thickness = 100 nm) were deposited onto the active material by thermal evaporation (base pressure $<5 \times 10^{-6}$ mbar; UNIVEX 350 G, Leybold) through a shadow mask. The active area of a PV device was 2 × 2 mm^2, as defined by the overlap of the Al top electrode and the ITO bottom electrode. The perovskite PVs were encapsulated to allow for ambient-air operation using a procedure outlined in Refs. [63,76]. In short, a glass slide (Menzel GmbH, thickness 0.1 mm) was attached to the PV substrate using a single-component, UV-curable, and low-viscosity epoxy (Ossila), which subsequently was cured by 15 min exposure to UV light. The current–density–voltage characterization was performed under 1-sun illumination (AM 1.5G, 100 mW cm^{-2}, PVIV 94023A equipped with reference cell 91150V, Oriel Instruments), whereas the external quantum efficiency was measured with a monochromator system (Oriel Instruments). The thickness of the films was measured with a stylus profilometer (DektakXT, Bruker) and calculated as the average of three different measurements on different locations of the film.

Two catalyst electrodes were mounted on glass support structures, as described previously, and connected by wires to a 3-serial perovskite PV assembly to form the artificial-leaf device. Two wired catalyst electrodes were submerged into a 0.1 M KOH aqueous solution and positioned at an interelectrode distance of 1 cm. The perovskite PV assembly was illuminated with 1 sun (AM 1.5, 100 mW cm^{-2}) light and the produced current was measured with a Keithley 2400 source measure unit.

Supporting Information

Supporting Information is available from the Wiley Online Library or from the author.

Acknowledgements

T.S., C.L., and J.W. contributed equally to this work. This work was supported by the Artificial Leaf Project Umeå (K&A Wallenberg foundation, KAW 2011.0055), The Solar Fuels Umeå Strong Research Environment (Umeå University), the Swedish Research Council (grant dnr 2013-5252), and Energimyndigheten (36648-1 to JM and P34145-2 to LE). The authors also thank Ångpanneföreningen (TW) and Kempe foundations (TS and CL) for support, and acknowledge the facilities and technical assistance of the Umeå Core Facility Electron Microscopy (UCEM), and the Core facility for Vibrational spectroscopy (VISP) at the Chemical Biological Centre (KBC), Umeå University. The XPS measurements and analysis were done by Andrey Shchukarev.

Received: April 7, 2016
Revised: June 13, 2016
Published online: July 19, 2016

[1] T. Faunce, S. Styring, M. R. Wasielewski, G. W. Brudvig, A. W. Rutherford, J. Messinger, A. F. Lee, C. L. Hill, H. deGroot, M. Fontecave, D. R. MacFarlane, B. Hankamer, D. G. Nocera, D. M. Tiede, H. Dau, W. Hillier, L. Wang, R. Amal, *Energy Environ. Sci.* **2013**, *6*, 1074.
[2] N. S. Lewis, D. G. Nocera, *Proc. Natl. Acad. Sci. USA* **2006**, *103*, 15729.
[3] G. F. Moore, G. W. Brudvig, *Annu. Rev. Condens. Matter Phys.* **2011**, *2*, 303.
[4] D. Gust, T. A. Moore, A. L. Moore, *Acc. Chem. Res.* **2009**, *42*, 1890.
[5] L. Sun, L. Hammarstrom, B. Akermark, S. Styring, *Chem. Soc. Rev.* **2001**, *30*, 36.
[6] E. S. Andreiadis, P.-A. Jacques, P. D. Tran, A. Leyris, M. Chavarot-Kerlidou, B. Jousselme, M. Matheron, J. Pécaut, S. Palacin, M. Fontecave, V. Artero, *Nat. Chem.* **2013**, *5*, 48.
[7] S. A. Bonke, M. Wiechen, D. R. MacFarlane, L. Spiccia, *Energy Environ. Sci.* **2015**, *8*, 2791.
[8] P. Bogdanoff, D. Stellmach, O. Gabriel, B. Stannowski, R. Schlatmann, R. Krol, S. Fiechter, *Energy Technol.* **2016**, *4*, 230.

[9] S. Esiner, R. E. M. Willems, A. Furlan, W. Li, M. M. Wienk, R. A. J. Janssen, *J. Mater. Chem. A* **2015**, *3*, 23936.
[10] M. G. Walter, E. L. Warren, J. R. McKone, S. W. Boettcher, Q. Mi, E. A. Santori, N. S. Lewis, *Chem. Rev.* **2010**, *110*, 6446.
[11] D. G. Nocera, *Acc. Chem. Res.* **2012**, *45*, 767.
[12] A. R. Bin, M. Yusoff, J. Jang, *Chem. Commun.* **2016**, *52*, 5824.
[13] K. Fujii, S. Nakamura, M. Sugiyama, K. Watanabe, B. Bagheri, Y. Nakano, *Int. J. Hydrogen Energy* **2013**, *38*, 14424.
[14] J. Luo, J.-H. Im, M. T. Mayer, M. Schreier, M. K. Nazeeruddin, N.-G. Park, S. D. Tilley, H. J. Fan, M. Grätzel, *Science* **2014**, *345*, 1593.
[15] C. R. Cox, J. Z. Lee, D. G. Nocera, T. Buonassisi, *Proc. Natl. Acad. Sci. U S A* **2014**, *111*, 14057.
[16] T. J. Jacobsson, V. Fjallstrom, M. Sahlberg, M. Edoff, T. Edvinsson, *Energy Environ. Sci.* **2013**, *6*, 3676.
[17] M. Liu, M. B. Johnston, H. J. Snaith, *Nature* **2013**, *501*, 395.
[18] A. Kojima, K. Teshima, Y. Shirai, T. Miyasaka, *J. Am. Chem. Soc.* **2009**, *131*, 6050.
[19] Y. Zhou, O. S. Game, S. Pang, N. P. Padture, *J. Phys. Chem. Lett.* **2015**, *6*, 4827.
[20] C. D. Bailie, M. G. Christoforo, J. P. Mailoa, A. R. Bowring, E. L. Unger, W. H. Nguyen, J. Burschka, N. Pellet, J. Z. Lee, M. Gratzel, R. Noufi, T. Buonassisi, A. Salleo, M. D. McGehee, *Energy Environ. Sci.* **2015**, *8*, 956.
[21] N. Kedem, T. M. Brenner, M. Kulbak, N. Schaefer, S. Levcenko, I. Levine, D. Abou-Ras, G. Hodes, D. Cahen, *J. Phys. Chem. Lett.* **2015**, *6*, 2469.
[22] J. Burschka, N. Pellet, S.-J. Moon, R. Humphry-Baker, P. Gao, M. K. Nazeeruddin, M. Gratzel, *Nature* **2013**, *499*, 316.
[23] M. A. Green, K. Emery, Y. Hishikawa, W. Warta, E. D. Dunlop, *Prog. Photovoltaics Res. Appl.* **2015**, *23*, 1.
[24] L. Trotochaud, J. K. Ranney, K. N. Williams, S. W. Boettcher, *J. Am. Chem. Soc.* **2012**, *134*, 17253.
[25] R. Subbaraman, D. Tripkovic, K.-C. Chang, D. Strmcnik, A. P. Paulikas, P. Hirunsit, M. Chan, J. Greeley, V. Stamenkovic, N. M. Markovic, *Nat. Mater.* **2012**, *11*, 550.
[26] A. Singh, S. L. Y. Chang, R. K. Hocking, U. Bach, L. Spiccia, *Catal. Sci. Technol.* **2013**, *3*, 1725.
[27] M. Gong, W. Zhou, M.-C. Tsai, J. Zhou, M. Guan, M.-C. Lin, B. Zhang, Y. Hu, D.-Y. Wang, J. Yang, S. J. Pennycook, B.-J. Hwang, H. Dai, *Nat. Commun.* **2014**, *5*, 4695.
[28] M. D. Merrill, R. C. Dougherty, *J. Phys. Chem. C* **2008**, *112*, 3655.
[29] H. Shi, G. Zhao, *J. Phys. Chem. C* **2014**, *118*, 25939.
[30] B. Zhang, F. Li, F. Yu, X. Wang, X. Zhou, H. Li, Y. Jiang, L. Sun, *ACS Catal.* **2014**, *4*, 804.
[31] J. H. Alstrum-Acevedo, M. K. Brennaman, T. J. Meyer, *Inorg. Chem.* **2005**, *44*, 6802.
[32] D. K. Bediako, B. Lassalle-Kaiser, Y. Surendranath, J. Yano, V. K. Yachandra, D. G. Nocera, *J. Am. Chem. Soc.* **2012**, *134*, 6801.
[33] J. Jiang, A. Zhang, L. Li, L. Ai, *J. Power Sources* **2015**, *278*, 445.
[34] X. Zhu, C. Tang, H.-F. Wang, Q. Zhang, C. Yang, F. Wei, *J. Mater. Chem. A* **2015**, *3*, 24540.
[35] W. T. Hong, M. Risch, K. A. Stoerzinger, A. Grimaud, J. Suntivich, Y. Shao-Horn, *Energy Environ. Sci.* **2015**, *8*, 1404.
[36] X. Cui, P. Ren, D. Deng, J. Deng, X. Bao, *Energy Environ. Sci.* **2016**, *9*, 123.
[37] I. Zaharieva, M. M. Najafpour, M. Wiechen, M. Haumann, P. Kurz, H. Dau, *Energy Environ. Sci.* **2011**, *4*, 2400.
[38] A. Kleidon, L. Miller, F. Gans, V. Krewald, M. Retegan, D. A. Pantazis, P. Kurz, K. Takanabe, F. E. Osterloh, R. Marschall, D. K. Bediako, A. M. Ullman, D. G. Nocera, G. Dodekatos, S. Schünemann, H. Tüysüz, C. K. Chan, H. Tüysüz, A. Braun, C. Ranjan, F. L. Mantia, B. K. Miller, L. Zhang, P. A. Crozier, J. A. Haber, J. M. Gregoire, H. S. Park, A. S. Batchellor, L. Trotochaud, S. W. Boettcher, Solar Energy for Fuels, *371*, Springer International Publishing, **2016**.
[39] J. Brillet, J.-H. Yum, M. Cornuz, T. Hisatomi, R. Solarska, J. Augustynski, M. Graetzel, K. Sivula, *Nat. Photonics* **2012**, *6*, 824.
[40] H. Wang, H.-W. Lee, Y. Deng, Z. Lu, P.-C. Hsu, Y. Liu, D. Lin, Y. Cui, *Nat. Commun.* **2015**, *6*, 7261.
[41] M. G. Kibria, F. A. Chowdhury, S. Zhao, B. AlOtaibi, M. L. Trudeau, H. Guo, Z. Mi, *Nat. Commun.* **2015**, *6*, 6797.
[42] L. Liao, Q. Zhang, Z. Su, Z. Zhao, Y. Wang, Y. Li, X. Lu, D. Wei, G. Feng, Q. Yu, X. Cai, J. Zhao, Z. Ren, H. Fang, F. Robles-Hernandez, S. Baldelli, J. Bao, *Nat. Nano* **2014**, *9*, 69.
[43] T. Sharifi, E. Gracia-Espino, X. Jia, R. Sandström, T. Wågberg, *ACS Appl. Mater. Interfaces* **2015**, *7*, 28148.
[44] S. Cobo, J. Heidkamp, P. A. Jacques, J. Fize, V. Fourmond, L. Guetaz, B. Jousselme, V. Ivanova, H. Dau, S. Palacin, M. Fontecave, V. Artero, *Nat. Mater.* **2012**, *11*, 802.
[45] E. Gracia-Espino, F. López-Urías, H. Terrones, M. Terrones, *J. Phys. Chem. C* **2015**, *119*, 741.
[46] E. Gracia-Espino, X. Jia, T. Wågberg, *J. Phys. Chem. C* **2014**, *118*, 2804.
[47] J. D. Wiggins-Camacho, K. J. Stevenson, *J. Phys. Chem. C* **2009**, *113*, 19082.
[48] A. K. Das, R. K. Layek, N. H. Kim, D. Jung, J. H. Lee, *Nanoscale* **2014**, *6*, 10657.
[49] M. N. Iliev, P. Silwal, B. Loukya, R. Datta, D. H. Kim, N. D. Todorov, N. Pachauri, A. Gupta, *J. Appl. Phys.* **2013**, *114*, 033514.
[50] L. Huang, D. Chen, Y. Ding, S. Feng, Z. L. Wang, M. Liu, *Nano Lett.* **2013**, *13*, 3135.
[51] Z.-Q. Liu, K. Xiao, Q.-Z. Xu, N. Li, Y.-Z. Su, H.-J. Wang, S. Chen, *RSC Adv.* **2013**, *3*, 4372.
[52] T. Sharifi, F. Nitze, H. R. Barzegar, C.-W. Tai, M. Mazurkiewicz, A. Malolepszy, L. Stobinski, T. Wågberg, *Carbon* **2012**, *50*, 3535.
[53] W. Li, L. Xin, X. Xu, Q. Liu, M. Zhang, S. Ding, M. Zhao, X. Lou, *Sci. Rep.* **2015**, *5*, 9277.
[54] T. Zhao, C. Hou, H. Zhang, R. Zhu, S. She, J. Wang, T. Li, Z. Liu, B. Wei, *Sci. Rep.* **2014**, *4*, 5619.
[55] I. Stamatin, A. Morozan, A. Dumitru, V. Ciupina, G. Prodan, J. Niewolski, H. Figiel, *Phys. E (Amsterdam, Neth.)* **2007**, *37*, 44.
[56] M. S. Burke, L. J. Enman, A. S. Batchellor, S. Zou, S. W. Boettcher, *Chem. Mater.* **2015**, *27*, 7549.
[57] X. Lv, Y. Zhu, H. Jiang, X. Yang, Y. Liu, Y. Su, J. Huang, Y. Yao, C. Li, *Dalton Trans.* **2015**, *44*, 4148.
[58] H. Cheng, Y.-Z. Su, P.-Y. Kuang, G.-F. Chen, Z.-Q. Liu, *J. Mater. Chem. A* **2015**, *3*, 19314.
[59] F. Song, X. Hu, *Nat. Commun.* **2014**, *5*, 4477.
[60] N. Han, F. Zhao, Y. Li, *J. Mater. Chem. A* **2015**, *3*, 16348.
[61] M. Wang, Z. Wang, X. Yu, Z. Guo, *Int. J. Hydrogen Energy* **2015**, *40*, 2173.
[62] J. R. McKone, B. F. Sadtler, C. A. Werlang, N. S. Lewis, H. B. Gray, *ACS Catal.* **2013**, *3*, 166.
[63] A. Asadpoordarvish, A. Sandstrom, S. Tang, J. Granstrom, L. Edman, *Appl. Phys. Lett.* **2012**, *100*, 193508.
[64] N. J. Jeon, J. H. Noh, W. S. Yang, Y. C. Kim, S. Ryu, J. Seo, S. I. Seok, *Nature* **2015**, *517*, 476.
[65] A. Guerrero, J. You, C. Aranda, Y. S. Kang, G. Garcia-Belmonte, H. Zhou, J. Bisquert, Y. Yang, *ACS Nano* **2016**, *10*, 218.
[66] S. A. Bonke, M. Wiechen, D. R. MacFarlane, L. Spiccia, *Energy Environ. Sci.* **2015**, *8*, 2791.
[67] Q. Chen, H. Zhou, T.-B. Song, S. Luo, Z. Hong, H.-S. Duan, L. Dou, Y. Liu, Y. Yang, *Nano Lett.* **2014**, *14*, 4158.
[68] H.-L. Hsu, C.-P. Chen, J.-Y. Chang, Y.-Y. Yu, Y.-K. Shen, *Nanoscale* **2014**, *6*, 10281.
[69] S. N. Habisreutinger, T. Leijtens, G. E. Eperon, S. D. Stranks, R. J. Nicholas, H. J. Snaith, *Nano Lett.* **2014**, *14*, 5561.
[70] K. W. Tan, D. T. Moore, M. Saliba, H. Sai, L. A. Estroff, T. Hanrath, H. J. Snaith, U. Wiesner, *ACS Nano* **2014**, *8*, 4730.

[71] F. Machui, M. Hosel, N. Li, G. D. Spyropoulos, T. Ameri, R. R. Sondergaard, M. Jorgensen, A. Scheel, D. Gaiser, K. Kreul, D. Lenssen, M. Legros, N. Lemaitre, M. Vilkman, M. Valimaki, S. Nordman, C. J. Brabec, F. C. Krebs, *Energy Environ. Sci.* **2014**, *7*, 2792.
[72] T. M. Schmidt, T. T. Larsen-Olsen, J. E. Carlé, D. Angmo, F. C. Krebs, *Adv. Energy Mater.* **2015**, *5*, 1500569.
[73] A. Sandström, L. Edman, *Energy Technol.* **2015**, *3*, 329.
[74] Department of Energy, Fuel Cell Technologies Office Multi-Year Research, Development, and Demonstration Plan, http://energy.gov/eere/fuelcells/fuel-cell-technologies-office, accessed: April, 2016.
[75] R. Sander, *Atmos. Chem. Phys.* **2015**, *15*, 4399.
[76] A. Asadpoordarvish, A. Sandstrom, C. Larsen, R. Bollstrom, M. Toivakka, R. Osterbacka, L. Edman, *Adv. Funct. Mater.* **2015**, *25*, 3238.

